Trimethylphosphine-Assisted Surface Fingerprinting of Metal Oxide Nanoparticle by ^{31}P Solid-State NMR: A Zinc Oxide Case Study

Yung-Kang Peng,[†] Lin Ye,[†] Jin Qu,[†] Li Zhang,[‡] Yingyi Fu,[‡] Ivo F. Teixeira,[†] Ian James McPherson,[†] Heyong He,[‡] and Shik Chi Edman Tsang*,[†]

[†]The Wolfson Catalysis Centre, Department of Chemistry, University of Oxford, Oxford OX1 3QR, U.K.

[‡]Department of Chemistry and Shanghai Key Laboratory of Molecular Catalysis and Innovative Materials, Fudan University, Shanghai 200433, PR China

Ⓢ Supporting Information

ABSTRACT: Nano metal oxides are becoming widely used in industrial, commercial and personal products (semiconductors, optics, solar cells, catalysts, paints, cosmetics, sun-cream lotions, etc.). However, the relationship of surface features (exposed planes, defects and chemical functionalities) with physiochemical properties is not well studied primarily due to lack of a simple technique for their characterization. In this study, solid state ^{31}P MAS NMR is used to map surfaces on various ZnO samples with the assistance of trimethylphosphine (TMP) as a chemical probe. As similar to XRD giving structural information on a crystal, it is demonstrated that this new surface-fingerprint technique not only provides qualitative (chemical shift) but also quantitative (peak intensity) information on the concentration and distribution of cations and anions, oxygen vacancies and hydroxyl groups on various facets from a single deconvoluted ^{31}P NMR spectrum. On the basis of this technique, a new mechanism for photocatalytic •OH radical generation from direct surface—OH oxidation is revealed, which has important implications regarding the safety of using nano oxides in personal care products.
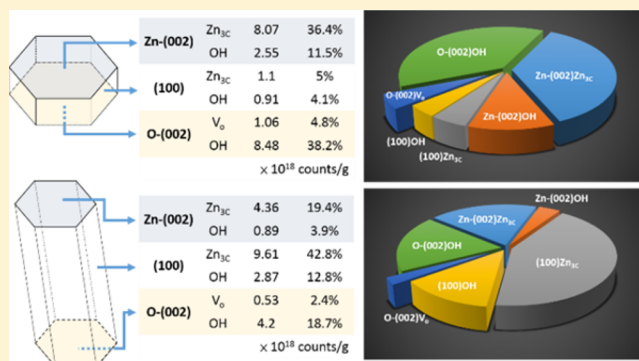
INTRODUCTION

Single-crystalline nanoparticles (NPs) with tailored facets show different physiochemical properties from their polycrystalline counterparts and have recently attracted much research interest.[1−9] Over the past decade, the variety of these materials has been actively expanded as their performance in fields such as optics,[1,2] electronic devices,[3,4] solar cells[5,6] and heterogeneous catalysis[7−9] is found to be greatly improved with the exposure of a specific facet. In particular, in the field of heterogeneous catalysis, which intrinsically involves the breakage and formation of chemical bonds between reactant and product at the catalyst surface, is closely associated with the coordination environment of the surface active atoms. The crystal facets exposed at the surface are, in turn, predominantly determined by the shape of the catalyst particle. For example, Pt (111) facets show much better methanol oxidation reactivity in fuel cell tests,[7] tetrahexahedral platinum NPs give superior electro-oxidation activity,[8] and the MgO (100) face plays a critical role in providing appropriate adsorption, molecular trafficking, and desorption during the benzylation of aromatics.[9] Since the active sites can be enriched and tuned by controlling particle morphology, the design and fabrication of single-crystalline NPs exposing a large fraction of targeted facets has been intensively pursued using a wide range of processing techniques, such as hydrolysis,[10] hydrothermal processing,[11]

microemulsion,[12] and thermal evaporation.[13] Ideally, the continuing development of these nanocatalysts with morphology-dependent activity would not only deepen understanding of the structural sensitivity of such catalysts, by correlating their reaction performance with their dominant crystal facet, but also bridge the gap between the model catalysts used in surface science and the real catalysts found in practical applications.

Often, however, comparison of such morphology-dependence is limited to individual studies, as the processing and post-treatment techniques used in the preparation of catalysts varies from group to group. This results in many differences between nanoparticles, in addition to the exposed facet, such as in the particle size distribution, extent of surface hydroxylation and particle homogeneity. Cross-literature comparison of NP catalysts is thus seriously hindered as there is currently no universal technique which can provide quantitative analysis of the concentration/distribution of surface features and the percentage of the desired facet on a given sample. For example, the tailoring of ZnO NPs to expose specific facets has been receiving increasing attention due to superior performances in solar cells and photocatalysis,[14−16] methanol synthesis,[17,18] optoelectronics[19] and gas sensing,[20] which were all attributed to

increased concentration of oxygen vacancies (V_O) on polar surface. However, there is currently no method to reliably characterize the facets, nor the V_O for a given ZnO crystallite. Photoluminescence (PL) and electron paramagnetic resonance (EPR) are the techniques most commonly used to reflect differences in V_O between samples, but they are not truly surface specific and are incapable of providing the concentration/distribution of V_O on specific facets. In fact, there have been disagreements between PL[21,22] and EPR[23,24] data in the literature.

Nuclear magnetic resonance (NMR) is a powerful technique that has been widely applied to study molecular physics, crystals and noncrystalline materials by providing a wealth of information about electronic interaction between atoms either in solution or in solid form. In general, solution NMR techniques offer higher resolution than those of solid state NMR, due to the absence of field inhomogeneity for species in solution. For example, characterization of metal colloid surfaces has recently been achieved by liquid phase ^{13}C NMR using formic acid as a chemical probe, although this method is restricted to some polymer stabilized metals which show fast tumbling motion in solution.[25] On the other hand, the use of probe molecules (e.g., ^{13}C-acetone for ^{13}C, trimethylphosphine (TMP) and trialkylphosphine oxides (R_3PO) for ^{31}P) in solid state NMR (ssNMR) has also been widely employed for the characterization of electronic interactions in solid structures as they can report on various microenvironments of solid surfaces.[26−28] In particular, use of the ^{31}P nucleus, with its 100% natural abundance and wide chemical shift range over 430 ppm, has been shown to be a sensitive and reliable technique capable of providing qualitative (type and strength) and quantitative (concentration) information on the discrete acid sites in various acid catalysts.[26] Even though this method is able to provide information on the active sites of working catalysts, knowledge of the distribution of these sites on various facets, which is key to understanding facet-dependent properties, is still lacking.

Herein, using ZnO as a model material, we report TMP-assisted surface mapping of oxide nanoparticles and crystallites using ^{31}P ssNMR and show that it is capable of providing comprehensive information (both qualitative and quantitative) on the surface features of various facets. As TMP, an electron donor molecule (Lewis base, LB), can form a stable adduct with the exposed cation of an oxide surface (Lewis acid, LA), the formation of a surface TMP-LA complex may be realized via coordination of the P atom to the LA center. It is shown that the ^{31}P chemical shift ($\delta^{31}P$) of the surface TMP-LA complex is able to differentiate between surface cations (Zn^{2+} or H^+) on facets at high resolution, with various Lewis acidities, surface energies and steric arrangements due to the stronger surface LA site pushing $\delta^{31}P$ to downfield. Single-crystalline plate- and rod-shaped ZnO nanoparticles containing preferentially exposed (002) and (100) facets, respectively and polycrystalline ZnO powder, were prepared to study the correlation between $\delta^{31}P$ and the adsorption configurations of TMP on various ZnO facets. Information such as the nature, binding strength and concentration of active sites on the various facets can thus be extracted from a single ^{31}P ssNMR spectrum. As a result, this technique, together with the as-built up ZnO facet fingerprint, not only provides quantitative information on surface features but also guides the rational design of facet-dependent nanocatalysis for a given sample. Using this technique in combination with density function theory (DFT) calculations,

we demonstrate facet and surface functionality-specific photocatalytic activity of ZnO nanocrystallites, and show how such an understanding may have important implications regarding the safe use of these nanoparticles in personal care products.

■ EXPERIMENTAL SECTION

Synthesis of ZnO Nanoplate. The synthesis of plate-like ZnO was based on our previous report.[17] 6.0 g zinc acetate dihydrate ($Zn(Ac)_2 \cdot 2H_2O$) and 3.84g hexamethylenetetramine (HMT, $C_6H_{12}N_4$) were dissolved in 48 mL deionized water. After a stirring of 10 min, the solution was transferred into a 100 mL Teflon-lined autoclave and maintained at 99 °C for 24 h. Then it was cooled to room temperature naturally. The white precipitate was collected by centrifugation at 5000 rpm for 10 min, after which the supernatant was decanted and discarded. The solid was washed repeatedly with ethanol and water to remove excess precursor. All ZnO nanoplate was dried in oven (100 °C) for 12 h and then calcined at 450 °C for 2 h (remove surfactant) with a heating rate of 10 °C/min in an air atmosphere.

Synthesis of ZnO Nanorod. To synthesize Rod-like ZnO was also prepared according to our previous report.[17] 1.487 g zinc nitrate hexahydrate ($Zn(NO_3)_2 \cdot 6H_2O$) and 6 g NaOH were dissolved in 10 mL deionized water (the molar ratio of Zn^{2+} to OH^- was 1:30). 100 mL ethanol was added to the Zn precursor solution. Five mL 1,2-ethanediamine (EDA) was also put into the mixture and then transferred to a covered plastic container with a volume capacity of 250 mL. The reaction container was kept at room temperature under constant stirring about 3 days. After the synthesis a white crystalline product was centrifuged and washed with deionized water and pure ethanol repeatedly. All ZnO nanorod was dried in oven (100 °C) for 12 h and then calcined at 450 °C for 2 h (remove surfactant) with a heating rate of 10 °C/min in an air atmosphere.

Synthesis of ZnO Nanopowder. The preparation of ZnO is similar to a method introduced by Tian et al. with a slight modification.[29] The evaporating dish with 28g of $Zn(Ac)_2 \cdot 2H_2O$ solid was placed into a furnace, for which the temperature was increased from room temperature to 450 °C with a heating rate of 10 °C/min in an air atmosphere and kept at the maximum temperature for 120 min. After naturally cooling to room temperature, the white powder was collected.

TMP-Adsorbed Sample Preparation. A typical vacuum line containing sample tube, TMP liquid tube and vacuum pump via isolation valves and pressure gauges were used (shown in Figure S1). Before loading the TMP molecules, 150 mg ZnO catalyst was placed in the sample tube and pretreated at 573 K for 1.5 h under vacuum (101 Pa) to ensure clean surface prior adsorption. After cooled down to room temperature, the sample tube was allowed to connect to the TMP liquid tube and thus TMP can be quickly vaporized under low pressure. 300 μmol/g-catalyst (calculated from the pressure and volume of isolated system) of TMP was introduced into solid sample which was kept in a liquid nitrogen jacket. As the surface acidity of our typical ZnO powders was in several tens μmol/g, the use of 300 μmol/g TMP was sufficient to saturate our samples. After 15 min equilibration, the sample was brought to ambient temperature in vacuum and thus excess nonadsorbed TMP molecules were removed gently for 2 min without affecting all the chemisorbed peaks. The sample tube was then flame-sealed and transferred to Bruker 4 mm ZrO2 rotor with a Kel-F end-cap in a glovebox under nitrogen atmosphere before the NMR measurement (shown in Figure S2).

Solid-State ^{31}P MAS NMR Experiments. Solid state magic angle spinning (MAS) NMR experiments were carried out using a Bruker Avance III 400WB spectrometer at room temperature. To remove the effect of proton spins on ^{31}P spectra, a strong radio frequency field (B) is usually applied in a pulsed at the resonance frequency of the nonobserved abundant spins (^{1}H herein) which contribute to the coupling of both spin species. If B is strong such that spins of ^{1}H is flipped rapidly compared with the spin−spin interactions, in the interaction is averaged to zero and consequently the excess broadening is zero. The high power decoupling (HPDEC) was thus used for the quantitative ^{31}P analysis. Considering the long relaxation time of [31]P

nuclei in NMR experiment, we used 30° pulse with the width of 1.20 μs, 15 s delay time. The radiofrequency for decoupling was 59 kHz. The spectral width was 400 ppm, from 200 to −200 ppm. The number of scanning was 800. The ^{31}P chemical shifts were reported relative to 85% aqueous solution of H_3PO_4, with $NH_4H_2PO_4$ as a secondary standard (0.81 ppm).

Computational Details. All calculations were performed in the framework of DFT by using the Vienna ab initio simulation package (VASP).[35−38] The projector-augmented wave (PAW) potentials[39,40] were used for the core electron interaction. The Perdew−Burke−Ernzerhof (PBE) function[41] based on the generalized gradient approximation (GGA) was employed to evaluate the nonlocal exchange-correlation energy. A plane wave basis set with a cutoff energy of 400 eV was used in all the optimizations. For structure optimization, the ionic positions were allowed to relax until the forces were less than 0.03 eV/Å. Spin polarization is included for all the calculations. The k-point grid determined by the Monkhorst−Pack method was 9 × 9 × 5 for ZnO bulk calculations in this study. The calculated lattice parameters of ZnO are 3.260 × 3.260 × 5.217 Å, which is in good agreement with the experimental value (3.249 × 3.249 × 5.205 Å). The ZnO surfaces were modeled by periodic slab models with three layers of ZnO repeat unit. The p(4 × 4) surface unit cells were used for polar Zn-(002) and O-(002). The dangling bonds of the Zn or O atoms in the bottom layers of polar surfaces were saturated by pseudohydrogens and all the atoms were relaxed during the calculation. A p(4 × 2) supercell was used for (100) surface and the bottom layer was fixed during all the calculations. The k-point grid of 2 × 2 × 1 was used in all the surfaces optimization and adsorption calculations. A vacuum layer of 12 Å along the z direction perpendicular to the surfaces (the x and y directions being parallel to the surface) was employed to prevent spurious interactions between the repeated slabs. The adsorptions of molecules on the ZnO surfaces were calculated as $E_{ads} = −(E_{slab+mol} − (E_{slab} + E_{mol}))$, in which E_{slab} and E_{mol} are the total energies of the ZnO slab and the single adsorbate molecule in gas phase; $E_{slab+mol}$ denotes the total energy of slab with adsorbed molecule. Chemical shift calculations for crystalline systems can be calculated using the linear response method. We used a typically higher cutoff energy of 500 eV and stopping criterion of 10−8 eV for electronic minimization. The isotropic chemical shift (δ_{iso}) is defined as $\delta_{iso} = \delta_{ref} − \delta_{cal}$, in which δ_{ref} is the reference chemical shift and δ_{cal} is the chemical shift result calculated by VASP. A chemical shift calculation of gas phase TMP was performed to obtain the reference chemical shift here.

Photocatalytic Activity Testing. Comparative catalytic testing was conducted at room temperature, with constant magnetic stirring to ensure full suspension of the particles throughout. An aqueous methylene blue (MB) stock solution (11.2 mg/L) was used for all photoreactions. 2.5 mg of ZnO sample was dispersed in 20 mL dye stock solution (11.2 mg/L catalyst concentration) and stirred for 30 min in the dark to allow dye adsorption/desorption to equilibrate. The reaction mixture was then exposed to irradiation with constant stirring in a Luzchem photoreactor fitted with 8 UVA lamps with nonmonochromatic irradiation centered at 350 nm resulting in a combined measured intensity of 4750 lx (Fc = 440). 1.5 mL samples of catalyst/dye solution were extracted at 5−10 min intervals and centrifuged at 4000 rpm for 5 min. Dye concentration was determined by tracking dye absorption at 664.5 nm using a PerkinElmer LAMBDA 750S UV/vis/NIR spectrophotometer after centrifuging each sample at 5000 rpm for 10 min to remove the suspended photocatalysts from solution. The decomposition of the dye over time was fitted to a pseudo-first-order rate equation $C = C_0 e^{−kt}$, where C = concentration at time t, C_0 = concentration at time t = 0, k = apparent rate constant (k_{app}) and t = irradiation time. Plotting $−\ln(C/C_0)$ vs irradiation time (t) results in a straight line with slope equal to k_{app}, which is a comparative measure of activity (kinetic efficiency) of the photoreaction.

RESULTS AND DISCUSSION

ZnO Nanocrystals. The syntheses of high quality ZnO nanocrystals with different morphologies are well documented in literature. Herein, we use single crystalline plate and rod ZnO NPs synthesized according to a procedure we reported previously[17] and polycrystalline powder ZnO NPs prepared by the calcination of $Zn(Ac)_2 \cdot 2H_2O$ at 450 °C for 2 h.[29] Figure 1
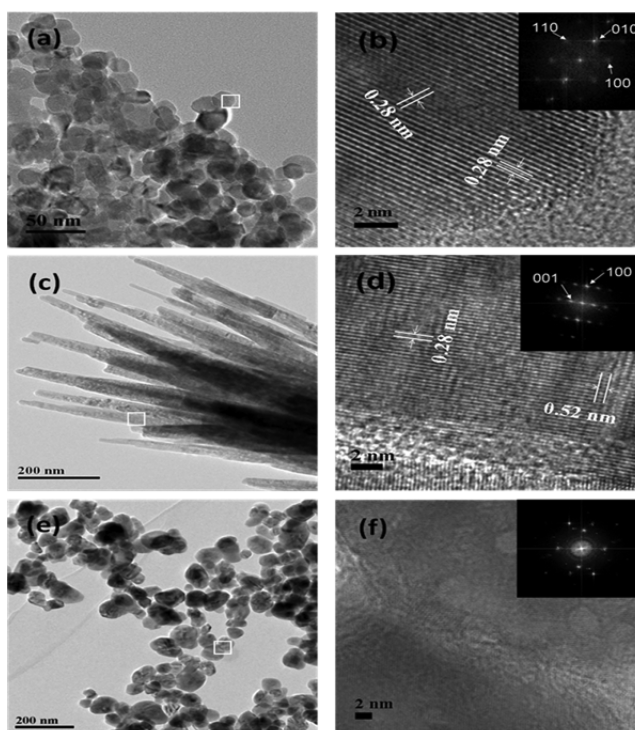

Figure 1. TEM and HRTEM images of ZnO (a, b) plate, (c, d) rod and (e, f) powder. Inset: corresponding electron diffraction (ED) pattern of ZnO plate, rod and powder.

shows transmission electron microscopy (TEM) images and electron diffraction (ED) patterns of as-prepared ZnO samples. The TEM image in Figure 1a reveals plate-shaped ZnO with diameters of 20−30 nm, and Figure 1c shows rod-shaped ZnO 600−800 nm long with diameters of 15−20 nm. In contrast, the powder sample (Figure 1e) shows irregular shapes with diameters in a wide range from 35 to 150 nm. As shown in Figure 2a, XRD analysis confirms that the three ZnO samples all show the wurtzite crystal structure (JCPDF 89−0511). The intensity of the (002) peak in the plates is higher than in the other morphologies, with this predominantly polar (002) facet covering the structure, whereas both rod and powder samples show relatively higher proportions of the nonpolar (100) and (101) planes. For single crystalline ZnO, it has been shown that a change in the relative intensity of the (100) and (002) peaks in the XRD patterns of the materials corresponds to a change in particle shape.[15] An intense (100) peak (corresponding to a small (002)/(100) ratio) indicates the formation of rod oriented along the c axis. Conversely, a high (002)/(100) ratio is indicative of shortening along the c axis and the presence of a large fraction of polar planes. Even though the XRD pattern of the powder sample is similar to that of the rod, as the powder sample was prepared without surfactant, its morphology is irregular and sphere-like owing to thermodynamic stability.[42] It is widely accepted that the growth of

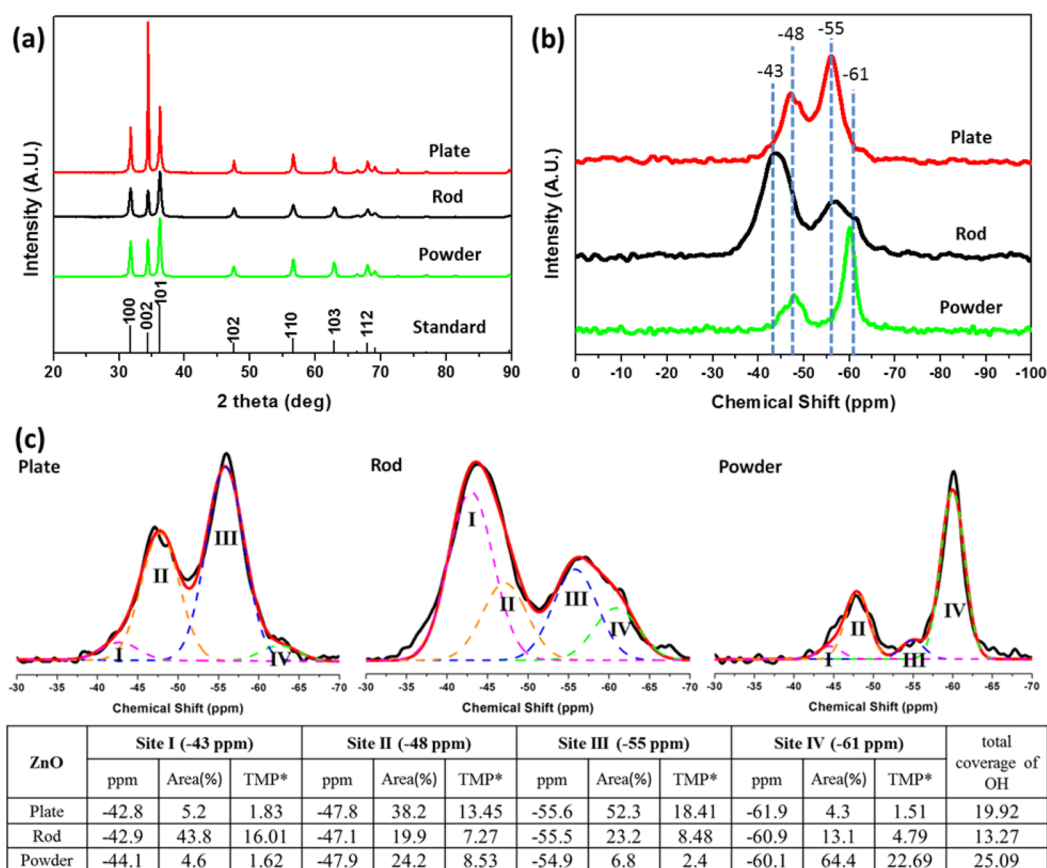| ZnO	Site I (-43 ppm)			Site II (-48 ppm)			Site III (-55 ppm)			Site IV (-61 ppm)			total coverage of OH
	ppm	Area(%)	TMP*	ppm	Area(%)	TMP*	ppm	Area(%)	TMP*	ppm	Area(%)	TMP*	
Plate	-42.8	5.2	1.83	-47.8	38.2	13.45	-55.6	52.3	18.41	-61.9	4.3	1.51	19.92
Rod	-42.9	43.8	16.01	-47.1	19.9	7.27	-55.5	23.2	8.48	-60.9	13.1	4.79	13.27
Powder	-44.1	4.6	1.62	-47.9	24.2	8.53	-54.9	6.8	2.4	-60.1	64.4	22.69	25.09

Figure 2. (a) XRD and (b) solid-state ^{31}P MAS NMR spectra (TMP adsorbed) of ZnO plate, rod and powder. (c) Spectral deconvolution of (b) and the corresponding data for each peak. *Adsorbed TMP molecules in μmol/g. The total coverage of OH on the surface was calculated from Site III and Site IV.

nanoparticle with no strong surface ligation will produce larger particle of low aspect ratios (spherical shape) due to thermodynamic driven stability (minimization of surface energy). On the other hand, a structural directing agent plays a critical role in shape control of colloidal nanoparticles since anisotropic shapes have larger surface area (cf. spherical shape), which renders them metastable, high-energy forms. Therefore, the formation of metastable shaped nanoparticles requires a kinetic growth control via chelation of structural directing agent. As the growth rate of a crystal facet depends on the surface energy (high-energy facets grow more quickly than low-energy facets), different morphologies of nanoparticle could thus be prepared by using various structural directing agents. For example, in this study, hexamethylenetetramine ($C_6H_{12}N_4$) and 1,2-ethanediamine were employed respectively in the preparation of nanoplate and nanorod.[42] According to the high-resolution TEM (HRTEM) image (Figure 1f) and the ED pattern (Figure 1f inset), the powder sample reveals polycrystallinity which is in stark contrast to the well-defined single crystalline structure of the plate (Figure 1b) and rod (Figure 1d). As evidenced by HRTEM measurements of the plate and rod, the lattice spacing a and c is calculated to be 0.28 and 0.52 nm, respectively, both matching the literature values.[30] For the plate, the two dominant surfaces are terminated by the (002) crystal plane but for rod the preferentially exposed surface is (100).

Surface Finger-Printing of ZnO Nanocrystals. Figure 2b shows the ^{31}P ssNMR spectra of TMP adsorbed on ZnO plate, rod and powder. In general, a stronger interaction of the surface

acidic site with the basic TMP molecule gives a more positive $\delta^{31}P$ shift in the NMR spectrum, the magnitude of the shift depending on the adsorption energy and adsorption geometry on a particular facet (vide infra). Notice that the separated desorption experiments were attempted on TMP-adsorbed plate (Figure S3a) and rod (Figure S3b) samples to determine the relative strengths of interaction with different TMP peaks. The intensity of the peak at −55 ppm was shown to decrease pronouncedly compared to the peak at −48 ppm (plate) and −43 ppm (rod), suggesting a weaker interaction with the TMP molecule under high vacuum (<0.1 Pa). Also, the peak at −61 ppm can be disappeared after the desorption at 20 °C under prolonged desorption time on the high vacuum (Figure S3c), suggesting that this signal came from the weakest adsorbed TMP on a surface hydroxyl group (OH).[26] It is interesting to note from Figure 2b that each sample reveals two large distinct ^{31}P resonances (−48 and −55 ppm for plate, −43 and −55 ppm for rod, −48 and −61 ppm for powder) in the range from −30 to −70 ppm. Generally, adsorbed TMP molecules can react with Brønsted Acid (BA) sites to form TMPH$^+$, giving rise to a $\delta^{31}P$ from −2 to −5 ppm, while TMP molecules bound to LA sites result in a $\delta^{31}P$ in the range from ca. −30 to −61 ppm (Figure S4).[26] Since no signal of TMPH$^+$ is detected in all the three ZnO samples, the peaks at −43, −48, −55, and −61 ppm can be initially assigned as the interactions between TMP and surface LA sites. The formation of a TMP-LA complex can be realized by the coordination of the P atom to a LA center; therefore, the lower the electron density on a LA site, the stronger the binding energy between TMP and LA site.[43] The

spectrum of each ZnO sample is thus deconvoluted into four components, namely Site I (−43 ppm), Site II (−48 ppm), Site III (−55 ppm) and Site IV (−61 ppm) and the concentration of adsorbed TMP on each site is calculated according to the corresponding peak area (Figure 2c). Notice that the raw spectra data of all three samples show a standard deviation of around ±0.5−1 ppm in chemical shift position. Accordingly, during the spectral deconvolution, we have fixed all four positions (i.e., −43, −48, −55, and −61 ppm) for all three samples within ±1 ppm uncertainty. To rationalize the nature of interactions giving rise to these peaks, adsorption energies/configurations of the basic TMP molecule on the acidic sites on each crystal facet are considered. DFT calculation of Bader charge shows that Zn_{4C} sites, in which Zn^{2+} is coordinated to 4 [O] atoms, possess the highest acidity (lowest electron density) on both the (100) and (002) facets (Figure S5). However, the lack of vacant sp^3 orbitals to bind the TMP, and the high energy required for transformation from tetrahedral sp^3 to trigonal bipyramidal dsp^3 geometry (Figure S6), means the formation of adduct bond with these sites is unlikely. Zn ions with lower coordination number (Zn_{2C}) exposed upon V_O formation ($Zn_{Vo(2C)}$) are also excluded due to their unfavorable formation energy (Figure S7 and Table S1). Thus, only surface unsaturated Zn_{3C} is thought to form adduct with TMP, resulting in its significant chemical shift.

As seen from Table 1, the DFT calculations of TMP adsorption energy and chemical shift of phosphorus on

Table 1. Calculated Adsorption Energy and Chemical Shift of TMP Adsorbed on Various Acidic Surface Features of ZnO; $(100)Zn_{3C}$: Zn_{3C} on (100) Facet; (100)Zn-OH: Hydroxyl Group on (100) Facet; $Zn-(002)Zn_{3C}$: Zn_{3C} on Zn-Terminated (002) Facet; Zn-(002)Zn-OH and O-(002)Zn-OH: Hydroxyl Group on Zn-/O-Terminated (002) Facet, Respectively

structure	$E_{adsorption}$ (eV) calc.	$\delta^{31}P$ (ppm) calc.	$\delta^{31}P$ (ppm)
$(100)Zn_{3C}$	−1.15	−41.97	−42.9
(100)Zn-OH	−0.01	−60.54	−60.9
$Zn-(002)Zn_{3C}$	−0.86	−[a]	−47.8
Zn-(002)Zn-OH	−0.45	−[a]	−55.6 (−55.1[b])
O-(002)Zn-OH	−0.57	−[a]	−55.6 (−53.0[b])

[a]The calculations for $\delta^{31}P$ are not reliable due to the effect of charge on the polar surfaces. [b]Calculated from linear regression of adsorption energy (Figure S8).

anticipated acidic surface sites (Zn_{3C} and OH) and facets were carried out and are summarized therein (further possible acid sites were considered in Table S2). It has been observed that both binding energy[43] and adsorption energy[25] of TMP molecule on Lewis acid site of ZnO show a strong correlation with its NMR chemical shift value. Indeed, our calculation of adsorption energy displays a linear relationship with the calculated chemical shift (Figure S8a). Notice that the calculated chemical shift of TMP on (100) Zn_{3C} (−41.97 ppm) matches well with experimental data from the rod sample with preferentially exposed (100) facets (−42.9 ppm) within a given error range. As (002) polar facets dominate in the plate sample and the population of O-(002)$Zn_{Vo(3C)}$ is minor (as it is mostly converted into O-(002)Zn-OH, Figure S9), the experimentally observed resonance at around −48 ppm (Site II) can be attributed to the interaction between TMP and Zn-

$(002)Zn_{3C}$ according to the corresponding calculated adsorption energy. The signal at −55 ppm of Site III is assigned to the adsorption of TMP on Zn-(002)Zn-OH and O-(002)Zn-OH which show comparable adsorption energies. The signal at −61 ppm of Site IV can be assigned to weak adsorption of TMP on nonpolar (100)Zn-OH or related surfaces.[26] Schematic illustrations of molecular interaction of these four sites (i.e., Site I, II, III and IV) are summarized in Figure 3. It is noted that the calculated adsorption energy of TMP on nonpolar (100)Zn-OH is only −0.01 eV, while this energy becomes 50 times higher (~0.5 eV) when the TMP interacts with a hydroxyl group on polar surface (compare Zn-(002)Zn-OH (−0.45 eV) and O-(002)Zn-OH (−0.57 eV)). It should be noted that the theoretical calculated adsorption energy (E_{ad}) of TMP on (100)Zn-OH (10 meV) is lower than the thermal energy (25 meV) based on our model with taken no account of thermal energy. However, according to our experimental data (Figure S8b), the E_{ad} of TMP on this surface feature gives 113 meV, which is higher than the thermal energy value. Thus, there is a discrepancy between theory and experiment in our work at present. Although it could be a complex issue, it is aimed to include thermal energy calculations in our theoretical models in future. According to both experimental and theoretical data, the interaction between hydroxyl protons and TMP seems highly dependent on the surface polarity of the ZnO facet. This preferential adsorption of molecules on a specific facet has been observed and is attributed to the difference in surface energy and surface atomic arrangement between facets.[42,44] Solid-state ^1H MAS NMR was used to probe the electron density of the hydroxyl protons. As shown in Figure S10, both plate and rod samples show a resonance peak at 4.8 ppm and two signals at smaller shift values between 0 and 2 ppm. Probing hydrogen in ZnO nanorods using solid-state ^1H MAS NMR, Wang et al. assigned the peak at 4.8 ppm to a strongly bonded proton in defect sites, as it was observed even after heating to 773 K, while the multiple chemical shifts between 0 and 2 ppm were assigned to water or surface hydroxyl groups, since they could be mostly removed upon heating to 573 K.[31] Accordingly, our chemical shift at 4.8 ppm comes from a hydroxyl proton on a polar surface, while the other two signals arise either from hydroxyl protons on nonpolar surface or physisorbed water (Figure S10). The simultaneous decrease in relative intensity of the peak at 4.8 ppm and increase of the peak between 0 and 2 ppm suggests an increase in the nonpolar surface at the expense of polar surface when the morphology is changed from plate to rod, which is in good agreement with the results obtained from ^{31}P MAS NMR. A comment on the discrepancy between the relative intensity of the XRD peaks (Figure 2a) for (100) and (002) facets and those obtained from NMR analysis (Figure 2b) is also discussed in Supporting Information (Figure S11).

By combining the information from Figure 2c and Figure 3, the relation between surface features and the configuration of adsorbed-TMP can be determined and several remarks made: (1) The TMP molecule binds to the (100) facet of the rod sample, giving a dominant chemical shift at −43 ppm (Site I). (2) For TMP adsorption on ZnO crystallites (i.e., plate or rod in this study), Site II (−48 ppm, Zn-(002)Zn_{3C}) appears to link with Site III (−55 ppm, Zn-(002)Zn-OH and O-(002)Zn-OH) with an area/intensity ratio of 1.3, indicating they come from the exposure of both positively Zn-/ negatively O-terminated polar surfaces. (3) For the polycrystalline powder, Site II (−48 ppm) comes from the adsorption of the TMP molecule on fully
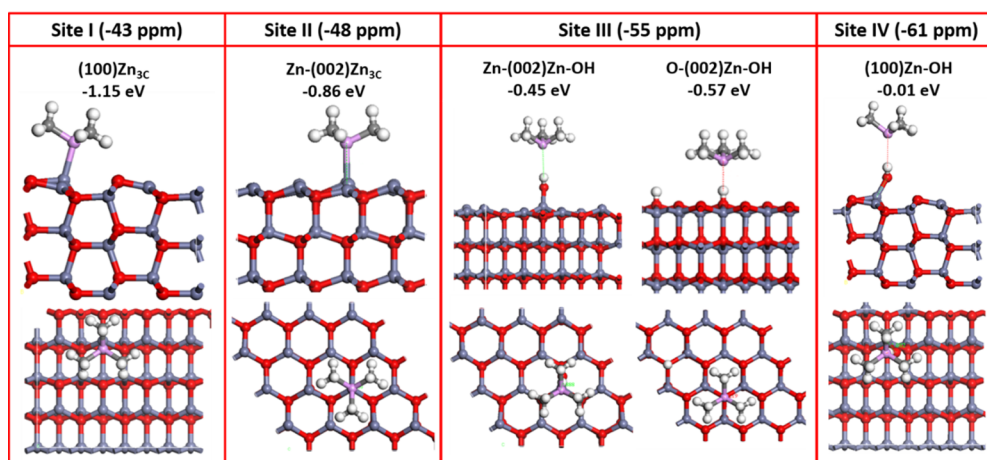
Figure 3. Schematic illustrations of molecular interaction and calculated adsorption energy between TMP and various surface features: $(100)Zn_{3C}$, $Zn-(002)Zn_{3C}$, $Zn/O-(002)Zn-OH$ and $(100)Zn-OH$.
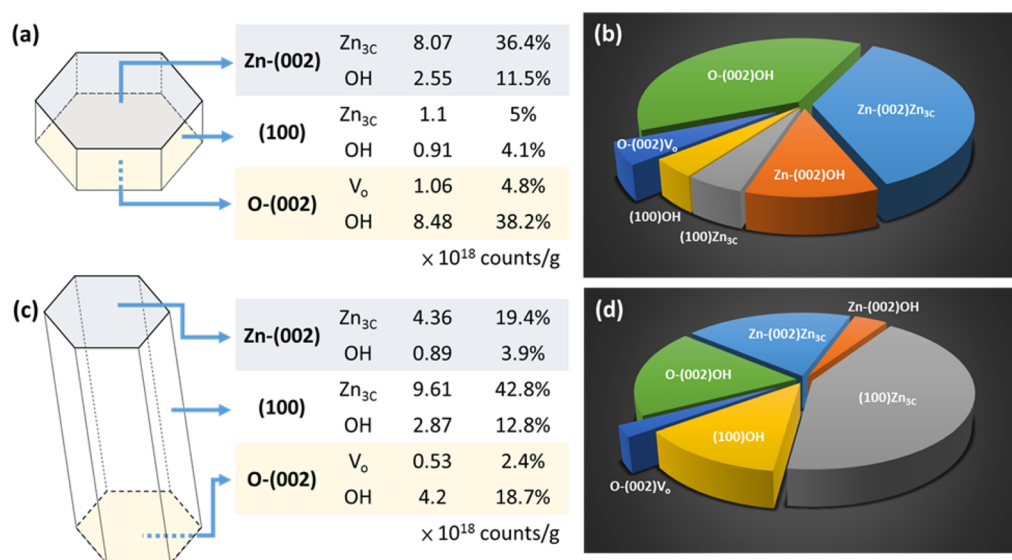

Figure 4. Distribution, concentration and percentage of surface features of NMR detected species on various ZnO facets of (a, b) plate and (c, d) rod. The concentrations of Zn_{4C} and [O] were not included.

exposed Zn ions at particle edges or corners, and is similar to the exposed zinc ion on polar $Zn-(002)Zn_{3C}$ sites (Figure 3). However, the peak intensity of Site III is remarkably low with an area/intensity ratio of 0.3, indicating TMP adsorption in this case does not adsorb on a polar surface. Compared to the low intensity of Site III (-55 ppm), the strong signal at Site IV (-61 ppm) in the powder sample also supports our discovery that the interaction between hydroxyl protons and TMP is affected by surface polarity. (4) For single-crystalline ZnO, the ratio of the peak area of Site II (-48 ppm) and Site I (-43 ppm) can act as an index to evaluate the percentage of exposed polar surface of the sample. For instance, the ratio for the plate sample is 7.25, which is 15 times more than that of rod sample (only 0.45). According to points (1) to (4), this technique (i.e., using TMP to probe crystal facets) can thus be a potential surface probe that not only provides quantitative information on acid sites, but is also as a powerful tool to evaluate their distribution on various exposed oxide facets.

To estimate the V_O concentration on the surface of these nanosize ZnO samples, we have to invoke some fundamental data derived from previous studies on the ZnO $O-(002)$ facet.

The high affinity of protons for 3-fold coordinated oxygen on the ZnO $O-(002)$ surface has been reported by Diebold et al.[32] By using STM and scanning tunneling spectroscopy (STS), they found that this surface is always saturated with hydrogen even under UHV conditions due to absence of metallization of this surface. On the other hand, Wöll's group studied the saturation coverage of protons as a function of temperature on ZnO $O-(002)$ by He atom scattering (HAS) using "H_2O adsorption probability measurement".[33] They showed that the saturation coverage of protons on $O-(002)$ at 300 K is around 0.8 ML (full saturation of protons is equal to 1 ML at temperatures below 200 K), while this value decreases to 0.2 ML when the temperature increases to 600 K. The decrease of the saturation coverage of protons was attributed to the generation of V_O by recombination of H atoms with OH-species (i.e., thermal desorption of water). Accordingly, we can therefore calculate the V_O concentration on the plate $O-(002)$ at room temperature by using the amount of OH on the polar surfaces determined from the NMR data(Figure 2c, Site III, 18.41 μmol of adsorbed TMP/g). First of all, the saturation coverage of protons (1 ML) on plate $O-(002)$ was calculated to
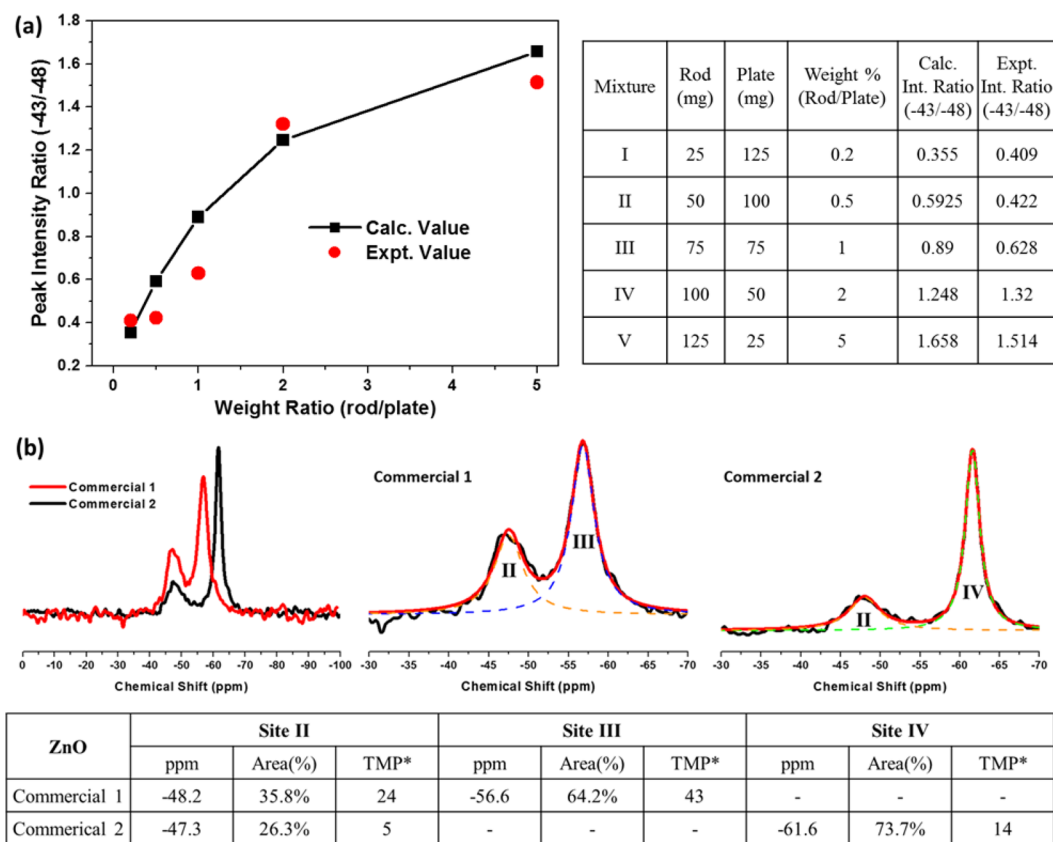
Figure 5. (a) The mixtures of plate/rod and the corresponding intensity ratio of peak −43 ppm and −48 ppm. Calc. value: using as-measured intensity ratio (−43/-48) of single component-plate/-rod sample to predict the signal intensity of their mixtures; Expt. value: the intensity ratio obtained from ssNMR spectrum of TMP-adsorbed mixture. (b) ^{31}P MAS NMR spectra of two ZnO commercial samples (TMP adsorbed) and the corresponding data of each deconvoluted peak. *Adsorbed TMP molecules in μmol/g.

be 1.06×10^{19} counts/g (see Supporting Information for detail). Since the coverage of OH is inversely proportional to the temperature[33] (Figure S12) and the generation of V_O is accompanied by thermal desorption of water, the V_O concentration on O-(002) can thus be calculated as a function of temperature. As shown in Table S3, the V_O concentration on plate O-(002) at room temperature was determined to be 1.06×10^{18} counts/g and this value increases to 4.24×10^{18} counts/g when the temperature is raised to 600 K. It should be noted that this is the first time the concentration of V_O at room temperature on a specific facet of ZnO has been derived from this new mapping technique. We can also calculate the number of TMP molecules adsorbed on Zn-(002)Zn-OH (2.55×10^{18} counts/g, 23%) and O-(002)Zn-OH (8.48×10^{18} counts/g, 77%), both of which contribute to the intensity of the peak at −55 ppm (Figure 3). The quantification and the distribution of various surface features on different facets of ZnO plate and rod at 300 K are summarized in Table S4 (powder was included) and in Figure 4. In order to verify whether this surface fingerprint can be used to assess the degree of exposed facets for a given ZnO sample, we prepared several mixtures with different ratios of the rod and the plate samples and analyzed them using the ratio of intensities at −43 ppm and −48 ppm. As shown in Figure 5a, except a small deviation in mixture II and III, the experimental data match the calculated values very well.

The ZnO facet fingerprint developed here is also found to be applicable to commercially available nano-ZnO samples. The deconvoluted ^{31}P MAS NMR spectra of two such commercially

available TMP-adsorbed ZnO samples following TMP-adsorption are shown in Figure 5b. From the spectra it can be seen that commercial sample 1 is similar to ZnO plate (Figure 2c) with a high Site III/Site II ratio (~1.8), indicating crystalline particles with a significant amount of exposed Zn-/O-terminated polar surfaces. Commercial sample 2, on the other hand, has a dominant ^{31}P resonance at −61 ppm similar to our powder sample and is expected to be polycrystalline with a high coverage of hydroxyl groups. The large degree of difference in crystallinity of the two commercial samples is further supported by HRTEM and electron diffraction studies (Figure S13).

Facet-Dependent Photocatalysis and Safety Implications. There is increasing evidence presented in the literature that photocatalytic activity is highly dependent on the particular facets exposed on transition metal oxide crystals. Using PL spectroscopy, Li et al. discovered a positive correlation between the polar faces exposed and the concentration of surface V_O of the samples.[15] The surface V_O of ZnO can act as potential wells to trap either one or two electrons, aiding electron−hole pair separation and hence increasing the photocatalytic activity. For decades, a high V_O concentration/exposed polar face has been regarded as the main criterion for high photocatalytic activity.[14,15] However, the surface V_O of ZnO is highly unstable when in contact with water, favoring for the formation of OH surface (Figure S9). Accordingly, photocatalytic decomposition of methylene blue in the presence of ZnO plate, rod and powder samples under ultraviolet irradiation was carried out to evaluate the facet-dependent catalytic activity (Figure 6a and
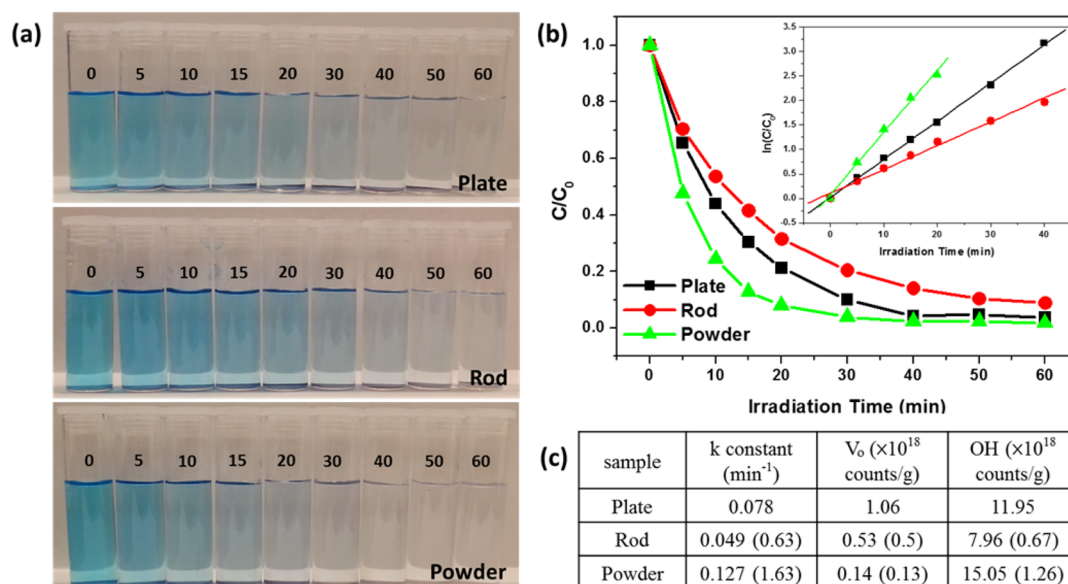
Figure 6. (a) Solution appearance of methylene blue versus UV irradiation time (min) and (b) corresponding photocatalytic activity of ZnO plate, rod and powder. (c) Summary of reaction rate constant, V_O and OH concentration of ZnO plate, rod and powder. For ease of comparison, the number in brackets shows the ratio of the parameter to that measured for plate.

sample	k constant (min^{-1})	V_O ($\times 10^{18}$ counts/g)	OH ($\times 10^{18}$ counts/g)
Plate	0.078	1.06	11.95
Rod	0.049 (0.63)	0.53 (0.5)	7.96 (0.67)
Powder	0.127 (1.63)	0.14 (0.13)	15.05 (1.26)

Figure S14). This reaction, monitored at 664.5 nm, followed pseudo-first-order reaction kinetics for all three samples (Figure 6b). According to previous results,[14,15] the exposure of a greater concentration of V_O leads to greater photocatalytic activity and is reflected in the reaction rate constant. As seen from the Figure 6c, for our crystalline samples, the plate with higher V_O concentration (1.06×10^{18} counts/g) indeed shows a higher rate constant ($k = 0.07793 \ min^{-1}$) while the lower rate constant of rod ($k = 0.04869 \ min^{-1}$) is associated with reduced V_O concentration (0.53×10^{18} counts/g). Surprisingly, our polycrystalline powder containing the lowest V_O concentration/polar surface according to our TMP NMR measurement in fact shows the highest reaction rate constant ($k = 0.127 \ min^{-1}$). Our BET characterization (Table S5) suggests the surface area of which was lower than the rod and plate samples. This indicates that the surface structure and composition, rather than surface area, are the key factors for the observed difference in the decomposition rates. The possibility of surface Zn_{3C} sites playing a key role is ruled out since the rod sample, possessing the highest concentration of Zn_{3C}, exhibits the lowest rate. This result also supports the conclusions of our previous study which found that the adsorption of dye molecules on Lewis acid sites (both V_O and Zn_{3C} herein) is not likely to be the rate-determining step for reaction in the ZnO case.[34] As O atoms in the surface lattice do not seem to take part in this catalyzed reaction, the concentration of surface hydroxyl group could be the key factor that overrides the role of V_O in the photocatalysis.

Figure 6c also compares the concentration of V_O and OH with corresponding rate constants from that of plate, rod and powder. The order reflected by the surface OH concentration clearly agrees with the rate constant, both being in the order powder > plate > rod. Moreover, comparison of the ratios of the rate constant, V_O and OH among three samples (in brackets, Figure 6c) suggests that surface OH plays a more critical role than V_O in the photocatalysis. Since the powder sample was prepared without surfactant, its surface should be mostly covered with OH, especially on corner or edge sites in

order to attenuate their higher surface energy. It is therefore understandable that polycrystalline powder with the lowest surface area (Table S5) possesses such a high surface OH concentration. On the other hand, the O-(002) polar surface is reported to be unstable due to electrostatic repulsion between oxygen atoms and tends to relax its surface energy through the formation of V_O and OH.[32,33] According to our surface mapping results ~80% of O atoms on O-(002) and ~20% of Zn atoms on Zn-(002) are in hydroxyl form at 300 K (Figure 4), the concentration of OH is proportional to exposed area of polar surfaces. Of the single-crystalline particles, the plate sample with a high percentage of polar facets (Table S4) shows a higher OH concentration and exhibits greater photocatalytic activity compared to the rod sample. Similar result have also been reported by Jang et al. and McLaren et al., who discovered that OH$^-$ ions prefer to adsorb onto polar faces due to the positive surface charge. These ions can react with holes (h$^+$) to generate reactive species •OH radicals, hence enhancing the photocatalytic activity.[14,16] Thus, from our NMR fingerprinting measurement, it is clear that the concentration of V_O may not be the primary cause for photocatalytic activity with surface OH coverage actually being responsible.

Generally, the recombination probability of the photogenerated carriers is high and therefore the lifetime of electron−hole pairs has been regarded as the most vital factor for the photocatalytic process.[33] Under light irradiation, electron transfer from the valence band (VB) to the conduction band occurs with the formation of electron−hole pairs on ZnO. In the case of ZnO with defects, these photogenerated holes can be trapped by surface defects and the separation of photogenerated electron−hole pairs is facilitated. Moreover, the photogenerated holes trapped by surface defects can also react with electron donors and thus promote the photocatalytic reaction. Since the existence of surface defects obviously play a positive role in the photocatalytic activity, tailoring the concentration of defects has received much attention during the past decade.[14−16] However, according to our result, the powder sample with the lowest V_O concentration exhibits the

highest rate constant, indicating the role of V_O in the charge separation and the preadsorption of dye is not as significant as previous reported. Since the recombination of a photogenerated electron−hole pair in ZnO occurs on the nanoscale time scale, the rate of electron/hole trapping must be faster than their diffusion, so that the species acting as the carrier traps must be preassociated with the chemical functionality of the photocatalyst surface.[33] Accordingly, it is the surface hydroxyl group instead of the adsorbed dye on V_O which is responsible for the generation of radicals. Figure S15 summarizes our proposed model for the enhanced photocatalysis over the Zn-OH surface. Once an electron in the Zn-OH bond is excited by light of an appropriate wavelength, transfer of the electron to the Zn^{2+} site takes place. The high potential of the photogenerated hole in the VB of ZnO (3.0 eV)[32] is adequate to oxidize surface OH groups directly to hydroxyl radicals ●OH (E° −OH/●OH = 2.4 eV). This OH radical will then be liberated from the surface and react with water to generate more radicals which eventually oxidize the methylene blue molecule. As water is the solvent, the OH group can be readily regenerated when the photoexcited conduction band electrons on Zn reduce water molecules accompanied by the generation of H_2. Thus, the overall catalytic reaction is $2H_2O \rightarrow 2$ ●OH + H_2.

As stated, nano-oxides including ZnO, Al_2O_3 and TiO_2 are beginning to be commercially explored as sunscreen lotions, cosmetics and personal care products with many desirable properties. However, their ability to generate radicals upon light illumination as discussed above, and the safety aspects associated with radical formation in close proximity to human skin, have been a major concern for the public. Using the technique reported herein, the exposure of polar surfaces are clearly found to be significant for photocatalytic radical generation; however, the high coverage of surface hydroxyl groups, especially in some commercial nano oxide samples we tested, can also generate a large quantity of radicals under light illumination. Regarding a large variation in crystallinity, size and surface functionality in commercial nano oxide samples that are currently available (Figure S13). Thus, their use in personal care products should be carefully assessed.

CONCLUSION

In summary, this surface fingerprinting technique using ^{31}P MAS NMR is able to provide unprecedented information on the concentration of cations, anions, V_O, and hydroxyl groups on both nonpolar and polar surfaces of ZnO nanoparticles. This technique is also applicable to other nanometal oxides and should enable systematic investigation of facet-dependent physiochemical properties in the future.

ASSOCIATED CONTENT

S Supporting Information

The Supporting Information is available free of charge on the ACS Publications website at DOI: 10.1021/jacs.5b12080.

> Detail setup for TMP-adsorption system and background information on ^{31}P MAS NMR analysis and peak assignment including DFT calculation of TMP adsorption energy and chemical shift, hydroxylation of Vo on O-(002); ^{1}H MAS NMR spectra of ZnO plate and rod; a discussion on the discrepancy in the relative intensity between XRD and NMR analysis; calculations of the concentration of surface features (Zn3C, OH, Vo) on

various facets; TEM and HRTEM images of two commercial ZnO samples; BET surface areas of ZnO plate, rod and powder; UV−vis absorption curves of methylene blue versus UV irradiation time with ZnO plate, rod and powder; schematic illustration of a proposed photocatalytic mechanism using surface hydroxyl group. (PDF)

AUTHOR INFORMATION

Corresponding Author

*edman.tsang@chem.ox.ac.uk

Notes

The authors declare no competing financial interest.

REFERENCES

(1) Huang, M. H.; Rej, S.; Chiu, C.-Y. *Small* **2015**, *11*, 2716−2726.
(2) Rej, S.; Wang, H.-J.; Huang, M.-X.; Hsu, S.-C.; Tan, C.-S.; Lin, F.-C.; Huang, J.-S.; Hunag, M. H. *Nanoscale* **2015**, *7*, 11135−11141.
(3) Dixit, H.; Zhou, W.; Idrobo, J.-C.; Nanda, J.; Cooper, V. R. *ACS Nano* **2014**, *8*, 12710−12716.
(4) Tan, C.-S.; Hsu, S.-C.; Ke, W.-H.; Chen, L.-J.; Huang, M. H. *Nano Lett.* **2015**, *15*, 2155−2160.
(5) Zhang, B.; Wang, D.; Hou, Y.; Yang, S.; Yang, X. H.; Zhong, J. H.; Liu, J.; Wang, H. F.; Hu, P.; Zhao, H. J.; Yang, H. G. *Sci. Rep.* **2013**, *3*, 1836−1843.
(6) Li, C.; Koenigsmann, C.; Ding, W.; Rudshteyn, B.; Yang, K. R.; Regan, K. P.; Konezny, S. J.; Batista, V. S.; Brudvig, G. W.; Schmuttenmaer, C. A.; Kim, J.-H. *J. Am. Chem. Soc.* **2015**, *137*, 1520−1529.
(7) Chrzanowski, W.; Wieckowski, A. *Langmuir* **1998**, *14*, 1967−1970.
(8) Tian, N.; Zhou, Z. Y.; Sun, S. G.; Ding, Y.; Wang, Z. L. *Science* **2007**, *316*, 732−735.
(9) Choudary, B. M.; Mulukutla, R. S.; Klabunde, K. J. *J. Am. Chem. Soc.* **2003**, *125*, 2020−2021.
(10) Jézéquel, D.; Guenot, J.; Jouini, N.; Fiévet, F. *J. Mater. Res.* **1995**, *10*, 77−83.
(11) Zhang, J.; Sun, L.; Yin, J.; Su, H.; Liao, C.; Yan, C. *Chem. Mater.* **2002**, *14*, 4172−4177.
(12) Guo, L.; Ji, Y. L.; Xu, H.; Simon, P.; Wu, Z. *J. Am. Chem. Soc.* **2002**, *124*, 14864−14865.
(13) Pan, Z. W.; Dai, Z. R.; Wang, Z. L. *Science* **2001**, *291*, 1947−1949.
(14) Jang, E. S.; Won, J. H.; Hwang, S.-J.; Choy, J. H. *Adv. Mater.* **2006**, *18*, 3309−3312.
(15) Li, G. R.; Hu, T.; Pan, G. L.; Yan, T. Y.; Gao, X. P.; Zhu, H. Y. *J. Phys. Chem. C* **2008**, *112*, 11859−11864.
(16) McLaren, A.; Valdes-Solis, T.; Li, G.; Tsang, S. C. *J. Am. Chem. Soc.* **2009**, *131*, 12540−12541.
(17) Liao, F.; Huang, Y.; Ge, J.; Zheng, W.; Tedsree, K.; Collier, P.; Hong, X.; Tsang, S. C. *Angew. Chem., Int. Ed.* **2011**, *50*, 2162−2165.
(18) Behrens, M.; Studt, F.; Kasatkin, I.; Kühl, S.; Hävecker, M.; Abild-Pedersen, F.; Zander, S.; Girgsdies, F.; Kurr, P.; Kniep, B.-L.; Tovar, M.; Fischer, R. W.; Nørskov, J. K.; Schlögl, R. *Science* **2012**, *336*, 893−897.
(19) Qin, Y.; Wang, X.; Wang, Z. L. *Nature* **2008**, *451*, 809−813.
(20) Wang, L.; Kang, Y.; Liu, X.; Zhang, S.; Huang, W.; Wang, S. *Sens. Actuators, B* **2012**, *162*, 237−243.
(21) Zhang, S. B.; Wei, S. H.; Zunger, A. *Phys. Rev. B: Condens. Matter Mater. Phys.* **2001**, *63*, 075205.

(22) Hu, J. Q.; Bando, Y. *Appl. Phys. Lett.* **2003**, *82*, 1401−1403.

(23) Garces, N. Y.; Giles, N. C.; Halliburton, L. E.; Cantwell, G.; Eason, D. B.; Reynolds, D. C.; Look, D. C. *Appl. Phys. Lett.* **2002**, *80*, 1334−1341.

(24) Djurišić, A. B.; Choy, W. C. H.; Roy, V. A. L; Leung, Y. H.; Kwong, C. Y.; Cheah, K. W.; Rao, T. K. G.; Chan, W. K.; Lui, H. F.; Surya, C. *Adv. Funct. Mater.* **2004**, *14*, 856−864.

(25) Tedsree, K.; Chan, C. W. A.; Jones, S.; Cuan, Q.; Li, W.-K.; Gong, X.-Q.; Tsang, S. C. E. *Science* **2011**, *332*, 224−228.

(26) Zheng, A.; Huang, S.-J.; Liu, S.-B.; Deng, F. *Phys. Chem. Chem. Phys.* **2011**, *13*, 14889−14901.

(27) Zheng, A.; Huang, S.-J.; Wang, Q.; Zhang, H.; Deng, F.; Liu, S.-B. *Chin. J. Catal.* **2013**, *34*, 436−491.

(28) Zheng, A.; Deng, F.; Liu, S.-B. Acidity Characterization of Solid Acid Catalysts by Solid-State 31P NMR of Adsorbed Phosphorus-Containing Probe Molecules. *Annual Reports on NMR Spectroscopy*; Elsevier, 2014; Vol. *81*, pp 47−108.

(29) Tian, C.; Zhang, Q.; Wu, A.; Jiang, M.; Liang, Z.; Jiang, B.; Fu, H. *Chem. Commun.* **2012**, *48*, 2858−2860.

(30) Djurišić, A. B.; Chen, X.; Leung, Y. H.; Ng, A. M. C. *J. Mater. Chem.* **2012**, *22*, 6526−6535.

(31) Wang, L.-Q.; Exarhos, G. J.; Windisch, C. F.; Yao, C.; Pederson, L. R.; Zhou, X.-D. *Appl. Phys. Lett.* **2007**, *90*, 173115.

(32) Diebold, U.; Koplitz, L. V.; Dulub, O. *Appl. Surf. Sci.* **2004**, *237*, 336−342.

(33) Kunat, M.; Girol, S. G.; Burghaus, U.; Wöll, C. *J. Phys. Chem. B* **2003**, *107*, 14350−14356.

(34) Zhao, Y.; Eley, C.; Hu, J.; Foord, J. S.; Ye, L.; He, H.; Tsang, S. C. E. *Angew. Chem., Int. Ed.* **2012**, *51*, 3846−3849.

(35) Fox, M. A.; Dulay, M. T. *Chem. Rev.* **1993**, *93*, 341−357.

(36) Kresse, G.; Hafner, J. *Phys. Rev. B: Condens. Matter Mater. Phys.* **1993**, *47*, 558−561.

(37) Kresse, G.; Hafner, J. *Phys. Rev. B: Condens. Matter Mater. Phys.* **1994**, *49*, 14251−14269.

(38) Kresse, G.; Furthmüller. *Phys. Rev. B: Condens. Matter Mater. Phys.* **1996**, *54*, 11169−11186.

(39) Blochl, P. E. *Phys. Rev. B: Condens. Matter Mater. Phys.* **1994**, *50*, 17953−17979.

(40) Kresse, G.; Joubert, D. *Phys. Rev. B: Condens. Matter Mater. Phys.* **1999**, *59*, 1758−1775.

(41) Perdew, J. P.; Burke, K.; Ernzerhof, M. *Phys. Rev. Lett.* **1996**, *77*, 3865−3868.

(42) Yin, Y.; Alivisatos, A. P. *Nature* **2005**, *437*, 664−670.

(43) Chu, Y.; Yu, Z.; Zheng, A.; Fang, H.; Zhang, H.; Huang, S.-J.; Liu, S.-B.; Deng, F. *J. Phys. Chem. C* **2011**, *115*, 7660−7667.

(44) Zhang, H.; Sun, J.; Dagle, V. L.; Halevi, B.; Datye, A. K.; Wang, Y. *ACS Catal.* **2014**, *4*, 2379−2386.